ADVANCED FUNCTIONAL MATERIALS
www.afm-journal.de

Thin-Sheet Carbon Nanomesh with an Excellent Electrocapacitive Performance

Huanjing Wang, Lei Zhi, Kaiqiang Liu, Liqin Dang, Zonghuai Liu, Zhibin Lei, Chang Yu, and Jieshan Qiu**

A facile yet effective chemical vapor deposition (CVD) method to prepare carbon nanomesh (CNM) with MgAl-layered double oxides (LDO) as sacrificial template and ferrocene as carbon precursor is reported. Due to the combined effect of the LDO template and organometallic precursor, the as-made hexagonal thin-sheet CNM features a hierarchical pore system consisting of micropores and small mesopores with a size range of 1–6 nm, and a great number of random large mesopores with a pore size of 10–50 nm. The density, geometry, and size of the pores are strongly dependent on the CVD time and the annealing conditions. As supercapacitor electrode, the CNM exhibits an enhanced capacitance, high rate capability, and outstanding cycling performance with a much-shortened time constant. The excellent capacitive performance is due to the presence of the large mesopores in the 2D CNM, which not only offer additional ion channels to accelerate the diffusion rate across the thin sheets but also help to make efficient use of the oxygen functional groups at the edges of large mesopores to increase the pseudocapacitance contribution.

1. Introduction

2D sheet-like materials represent an important family of electrode materials for electrochemical energy storage because of their large electrochemically active surface areas and short ion pathways.[1] Among various 2D materials, graphene has received ever-increasing attention due to its large theoretical surface area (2630 $m^2 g^{-1}$),[2] extraordinary electronic and mechanical property,[3] and unique 2D planar structure. However, a major problem in processing graphene electrodes is its easy aggregation into irreversible graphite via the strong sheet-to-sheet van der Waals attractions, resulting in a significant loss of ion-accessible surface area and a distinct increase of ion diffusion resistance, which subsequently leads to poor energy storage performance. To overcome the restacking problem and simultaneously to achieve a fast ion kinetic, porous graphene with different structures such as foams,[4–7] aerogels,[8] sponge-like structure,[9,10] and graphene-based hybridized materials[11–13] have been developed by template-assisted chemical vapor deposition (CVD), hydrothermal reduction, and electrostatic self-assembly methods. Nevertheless, the porosities in these graphene-based architectures are mainly in the form of pore/space between graphene layers, leading to a low charge storage capacity that cannot meet the requirement of a high-performance supercapacitor.

Most recently, graphene nanomesh (GNM) has emerged as one of the fascinating materials for application in field-effect transistors (FET)[14,15] and electrochemical energy storage.[16–18] The GNM features high-density nanopores on graphene-based 2D plane and large number of defective edges.[19,20] This kind of in-plane nanopores not only dramatically improves the charge storage capacity of graphene electrode but also substantially enhances the ion transport across the 2D graphene plane,[17,21–23] thus leading to the 3D ion diffusion mode within the electrode matrix. Introducing nanopores in the graphene planes can be accomplished by either nanoimprint lithography technique or chemical oxidation route. The lithography-based techniques show great versatility in precise control over both the periodicity and pore width, yielding GNMs with tunable electronic properties.[14,15,24,25] However, these fabrication techniques are time-consuming and complex. The cost-effective chemical route offers an alternative way for facile production of the GNMs in large scale, which relies on the local oxidation of carbon atoms with oxidants or catalysts to create vacancies on the graphene 2D plane.[16,22,26] Both the etching degree and the porosity can be readily manipulated by changing the etching time[27–29] or controlling the density and size of the catalyst on graphene sheets, at least to some degree.[30,31] However, in most

H. J. Wang, L. Zhi, Dr. K. Q. Liu, L. Q. Dang, Prof. Z. H. Liu, Prof. Z. B. Lei
Key Laboratory of Applied Surface and Colloid Chemistry
MOE and School of Materials Science and Engineering
Shaanxi Normal University
199 South Chang'an Road, Xi'an, Shaanxi 710119, P.R. China
E-mail: zblei@snnu.edu.cn
Dr. C. Yu, Prof. J. S. Qiu
Carbon Research Laboratory
Liaoning Key Lab for Energy Materials and Chemical Engineering
State Key Lab of Fine Chemicals
School of Chemical Engineering
Dalian University of Technology
Dalian 116024, P.R. China
E-mail: jqiu@dlut.edu.cn

DOI: 10.1002/adfm.201502025

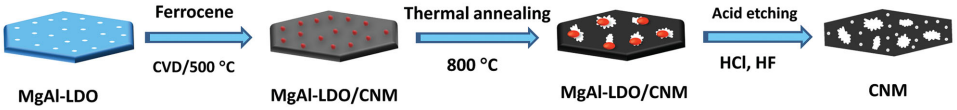

Scheme 1. Schematic illustration of the fabrication steps for CNM.

cases, the graphene materials used in these top-down routes are typically derived from chemically converted graphene, which usually possess severe structure defects and poor electrical conductivity. Moreover, the sheet stacking in these methods is still not easily prevented.

The template-assisted CVD is an effective bottom-up strategy for fabrication of porous graphene materials.[32–34] For example, by using porous MgAl-layered double oxide (LDO) or MgO with controllable structure as template, graphene nanofibers or protuberances-pillared graphene can be obtained.[34–36] However, the direct growth of GNMs on such inorganic template is difficult to be achieved,[17,32] and the precise control over the pore size, distribution, and pore density on the graphene plane still remains a big challenge. Herein, we report a facile CVD method to directly grow carbon nanomesh (CNM) on MgAl-LDO using ferrocene as carbon precursor. As illustrated in **Scheme 1**, the porous MgAl-LDO with a specific surface area (SSA) of 205 m^2 g^{-1} and a pore volume of 0.2 cm^3 g^{-1} derived by calcination of MgAl-LDH was adopted as template for the CNM growth. During the CVD process, the pyrolysis of ferrocene at 500 °C yielded carbon layers and ultrafine Fe particles that were homogenously deposited on the LDO surface. These Fe particles can be automatically converted to Fe_2O_3 once in contact with the MgAl-LDO. The LDO/carbon composite was subsequently heated at 800 °C. During this stage, the Fe_2O_3 particles grew in sizes, and etched away the carbon atoms nearby, yielding the vacancies on the carbon layers. The pore size, morphology, and pore density on the CNMs can be easily controlled by changing the CVD time and the thermal annealing conditions. Typically, two different carbon products, CNM and carbon nanosheet (CS) can be obtained, which are denoted as CNM*x*–*y* or CS*x*–*y*, where *x* is the CVD time (min) and *y* represents the annealing time (min) at 800 °C, respectively.

2. Results and Discussion

Figure 1a shows the scanning electron microscopy (SEM) images of the MgAl-LDO template, showing hexagonal flakes with a typical lateral size of 2–4 μm. Transmission electron microscopy (TEM) images (Figure S1, Supporting Information) show that the LDO contains a plenty of micropores, of which the formation is likely caused by the release of gaseous CO_2 and H_2O molecules during calcinating MgAl-LDH at 500 °C (Figure S1, Supporting Information),[37] leading to an increased SSA and pore volume as compared with those of MgAl-LDH (Table S1, Supporting Information). Figure 1b shows the SEM image of LDO/CNM60-90 composite. The carbon layers were uniformly deposited on the LDO surface to form a carbon layer–sealed LDO composite without damaging or destroying the hexagonal flake-like LDO. It should be noted that the expansion coefficients of LDO and carbon layers are different, which results in wrinkles and ripples on the carbon layers, as shown in Figure 1c. Figure 1d is the side-view SEM image of the thin carbon sheets (CSs) prepared by vacuum filtration of the dispersed carbon products. Unlike the severe aggregated structure as usually observed for chemically derived graphene,[38] the thin sheets with a thickness of 10 μm does not display compacted structure, suggesting that the restacking of the carbon layers has been effectively inhibited. A more detailed examination reveals that the thin sheet is actually made up of hexagonal carbon flakes (Figure 1e). Significantly differing from the rigid LDO and LDO/CNM composite, the curved carbon thin sheets are highly flexible, and oriented in random directions. The thin sheets display hollow interior structure with an edge thickness varying from 50 up to 90 nm (Figure 1f). Figure 1f shows that the carbon thin sheets are nearly transparent.

Figure 2 is the TEM images of the typical carbon thin sheets prepared in 60 min of the CVD time and 90 min of the annealing time. The carbon products are hexagonal flakes, resembling the morphology of pristine LDO template (Figure 2a). Interestingly, unlike the nonporous carbon flakes templated from LDO with CH_4 as precursor,[39,40] the carbon flakes or thin sheets fabricated in the present study are composed of irregular large mesopores that are randomly distributed on the surface of carbon thin sheets (Figure 2b). The presence of these large mesopores with a size varying from 10 to 50 nm (Figure 2c) suggests that the as-made carbon thin sheets are characteristic of carbon nanomesh (CNM60-90). Besides

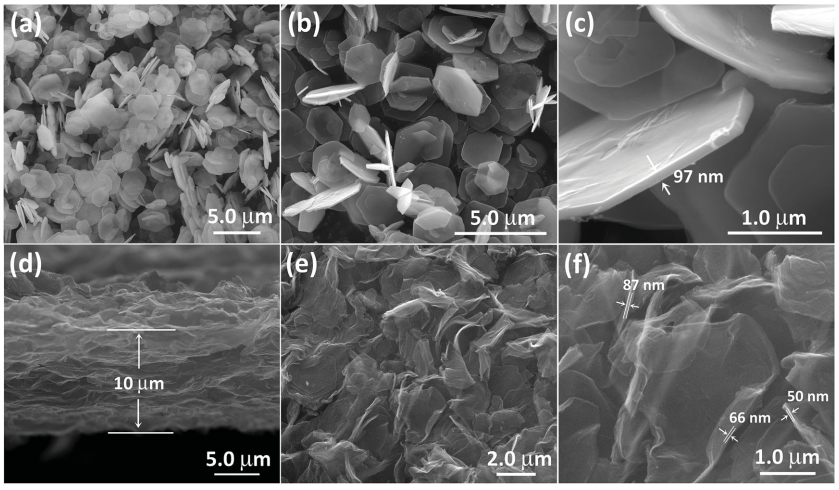

Figure 1. SEM images of a) LDO, b,c) LDO/CNM60-90, d) a film made up of CNM60-90, and e,f) the CNM60-90 with different magnifications.

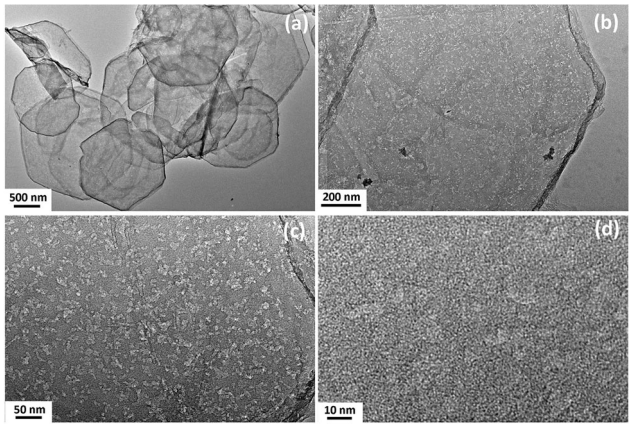

Figure 2. TEM images of CNM60-90 with a,b) low and c,d) high magnification.

these large mesopores, a high-resolution TEM in Figure 2d reveals that abundant micro- and mesopores can be seen in the surface of the carbon thin sheets. The existence of these well-defined micropores and mesopores is also evidenced by the N_2 adsorption isotherms (**Figure 3**a), where substantial N_2 uptake at $P/P_0 < 0.1$ and a pronounced hysteresis loop at $0.4 < P/P_0 < 0.7$ is clearly observed. According to the nonlocal density functional theory (NLDFT), the pore size in CNM60-90 distributes in two regions: 1–2 and 2–6 nm (Figure 3b). By comparing the pore size distribution (PSD) of LDO and CNM60-90, it can be concluded that these micro- and mesopores are generated from the porosity of LDO template. Due to the contribution of these micro- and mesopores, the SSA and pore volume of CNM60-90 reach 1440 $m^2 g^{-1}$ and 1.10 $cm^3 g^{-1}$, respectively, which is much higher than those of the LDO (Figure 3a and Table S1, Supporting Information). The surface chemistry of the CNM60-90 was probed by X-ray photoelectron spectroscopy (XPS) and Fourier-transform infrared spectroscopy (FTIR). Only C 1s and O 1s peaks were detected in the survey XPS spectrum (Figure S2, Supporting Information). The deconvoluted C 1s spectrum shows the presence of C—O (285.6 eV) and O=C—O (289.6 eV) groups (Figure 3c), which are consistent with the strong peaks of O—H (3461 cm^{-1}), C=O (1634 cm^{-1}), and C—O—C (1028 cm^{-1}) in FTIR spectra (Figure S3, Supporting Information).[41] These oxygen-containing groups are primarily located at the edges of large mesopores.[28,42,43] The atomic ratio of O/C in CNM60-90 is determined to be 6.9% according to the XPS analysis.

To figure out the formation mechanism of the larger mesopores in the carbon thin sheets, we examined the LDO/CNM composite by TEM and energy dispersive X-ray spectroscopy (EDX). **Figure 4** shows the dark-field TEM images and corresponding elemental mapping of Fe in LDO/CNM composites. The LDO/CNM samples were prepared at CVD time of 60 min (Figure 4a,b), followed by thermally annealed at 800 °C for 90 min (Figure 4c,d). Clearly, the Fe element is uniformly distributed in both samples. However, their sizes increase from ≈2 to 10–30 nm during the annealing stage (Figure 4b,d). The chemical composition of the element Fe was identified by XPS depth profile analysis. Figure 3d shows the XPS spectra of LDO/carbon composites annealed at 800 °C for 90 min. The corresponding composite without heat treatment is also included for comparison. It can be seen that both samples show two characteristic XPS peaks at 724.1 and 711.0 eV, which are associated

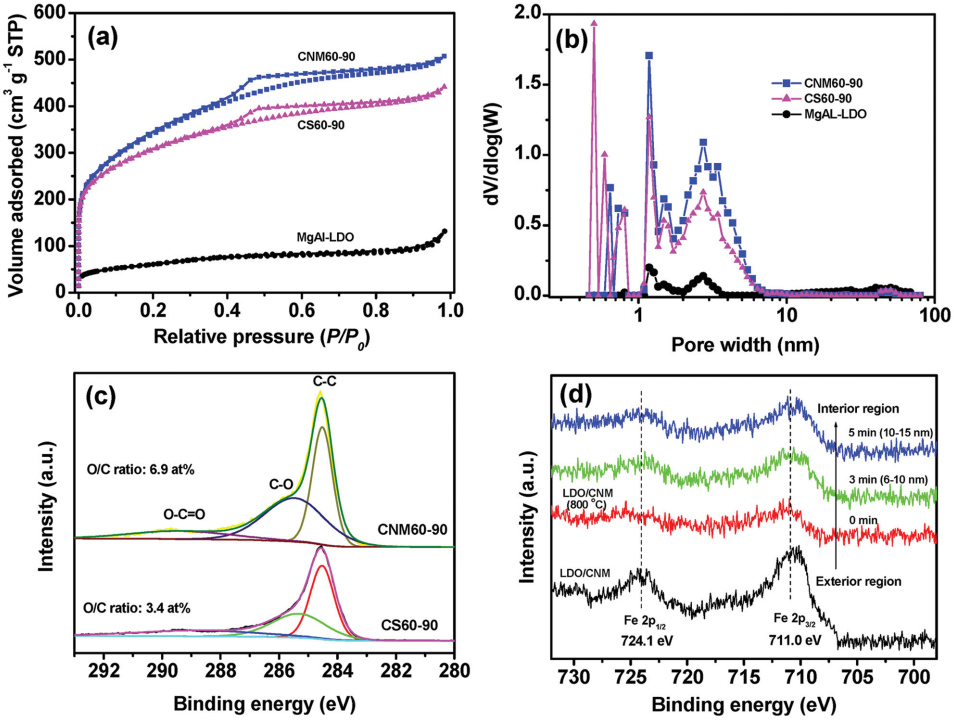

Figure 3. a) N_2 adsorption–desorption isotherm, b) PSD determined from NLDFT, c) deconvoluted C 1s XPS spectra of CS60-90 and CNM60-90, and d) Fe 2p XPS spectra of LDO/carbon samples prepared under different conditions.

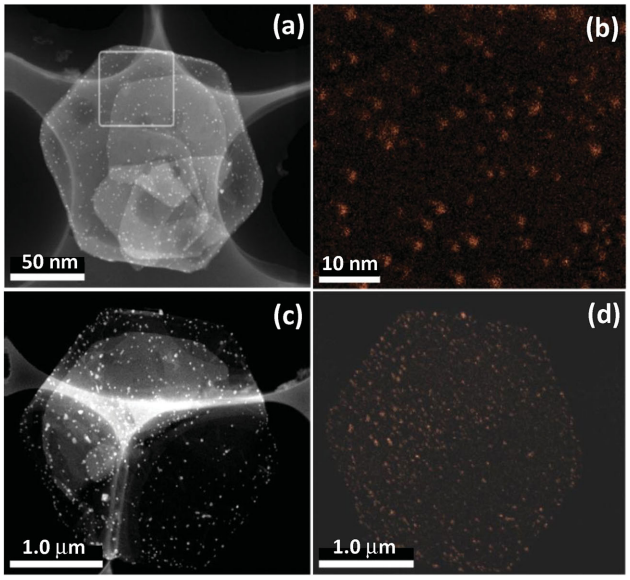

Figure 4. a,c) Dark-field TEM images and b,d) the corresponding element mapping of Fe for LDO/CNM a,b) prepared at CVD time of 60 min, c,d) followed by thermally annealed at 800 °C for 90 min.

to Fe $2p_{1/2}$ and Fe $2p_{3/2}$ of Fe_2O_3, respectively.[44] The lattice fringes of 0.28 nm are attributed to the (104) plane of hexagonal rhomb-centered Fe_2O_3 (JCPDF#89-0599), also confirms the Fe_2O_3 formation (Figure S4, Supporting Information). These results indicate that the ultrasmall Fe particles generated from the pyrolysis of ferrocene[45] could be spontaneously converted into Fe_2O_3 once in contact with LDO. The following thermal annealing of LDO/carbon does not change the oxidation state of the Fe species. The XPS depth profile analysis also reveals that these Fe_2O_3 particles are homogenously distributed on the exterior and in the interior of carbon thin sheets.

The amount of Fe_2O_3 particles embedded in the carbon matrix can be readily controlled by changing the CVD time. **Figure 5**a–c is the TEM images of LDO/CNM composites prepared at different CVD time, followed by heat treatment at 800 °C for 90 min. It can be seen that the number of Fe_2O_3 particles gradually increases with the CVD time. Apart from this

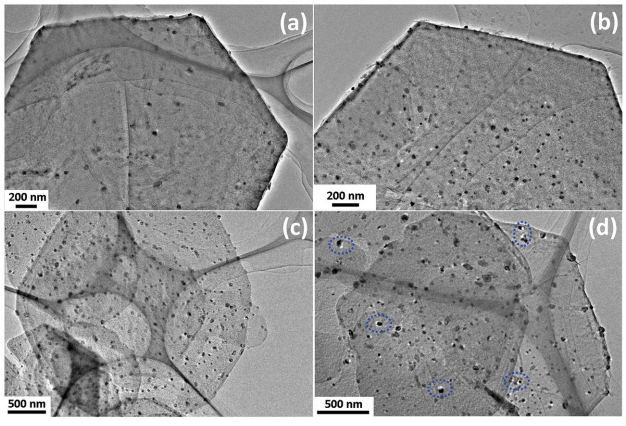

Figure 5. TEM images of a) LDO/CNM30-90, b) LDO/CNM60-90, c) LDO/CNM90-90, and d) LDO/CNM60-180.

variation, it is interesting to notice that there are some holes surrounding the Fe_2O_3 particles. This suggests that the oxidation of some carbon atoms have taken place at the peripheral of the Fe_2O_3–carbon contact region.[46,47] Figure 5d shows the LDO/CNM that was heated to a longer annealing time of 180 min, in which both the number and size of the holes around the Fe_2O_3 particles become more evident, implying the oxidation of carbon can be controlled to some degree by changing the annealing time of LDO/carbon composite at 800 °C.

As above discussed on the etching mechanism, the ability to control the number of Fe_2O_3 particles and the oxidation degree of the carbon matrix is of importance to tune the pore density and pore shape in the carbon thin sheets. **Figure 6**a–c shows the TEM images of the as-made CNM after removing the LDO template. It is seen that the number of the large mesopores increases distinctly with the CVD time. A statistical analysis by counting the pores with diameters over 10 nm reveals that the as-made CNM has a surface pore density of 0.65×10^3, 2.1×10^3, and 2.9×10^3 μm^{-2} at a CVD time of 30, 60, and 90 min, respectively. This pore density is slightly higher than 1.78×10^3 μm^{-2} of porous graphene created by controlled air oxidation,[28] and much higher than 5.0×10^9 cm^{-2} of graphene aerogel generated by a site-localized particle-induced etching strategy.[47] In addition, unlike the spherical Fe_2O_3 particles, most of the pores in the CNM are present as worm-like tracks. Moreover, the pore number in the CNMs is much higher than those of Fe_2O_3. Such observation might be related to the two reasons below: (i) in the TEM images of LDO/CNM composite (Figure 5), the LDO sealed by the carbon layers might interfere with the electron beam to detect the actual porous structure of CNM, and (ii) the track-like pores in the carbon thin sheets imply that each Fe_2O_3 particle does not merely function to create only one track-like pore because of their unbalanced motions during the thermal annealing stage.[31] In addition to the impact on the pore density of the CNMs, the CVD time also affects the SSA of the CNMs. As shown in **Figure 7**, the CNM30-90 has an SSA of 1781 m^2 g^{-1}, while in the case of CNM120-90 it drops to 959 m^2 g^{-1}. The decrease of SSA with the CVD time suggests that thicker carbon layers were deposited on the LDO, which is in agreement with the gradual increase of the products yields in longer CVD time (Figure 7).

To understand the impact of the annealing time on the pore structure, we compared the microstructure of CNM60-180 (Figure 6d–f) with those of CNM60-90 (Figure 6b). Both samples were prepared at the same CVD time but in different annealing time. Even after the heat treatment of LDO/carbon composite at 800 °C for 180 min, the CNM60-180 still preserves its macroscopically hexagonal flake-like structure (Figure 6d). However, a close examination reveals that the size of the large mesopores in carbon thin sheets dramatically increases to over 50 nm (Figure 6e,f). This pore enlargement suggests an excessive oxidation of carbon atoms by Fe_2O_3 in longer annealing time, and the merging of small pores into big ones during the annealing stage. To further elucidate how the large mesopores are formed, we have tried to remove the Fe_2O_3 particles and LDO with acid treatment before the thermal annealing of the LDO/carbon composite. Strikingly, in spite of the hexagonal structure being preserved, the products show totally different structures, which are composed of

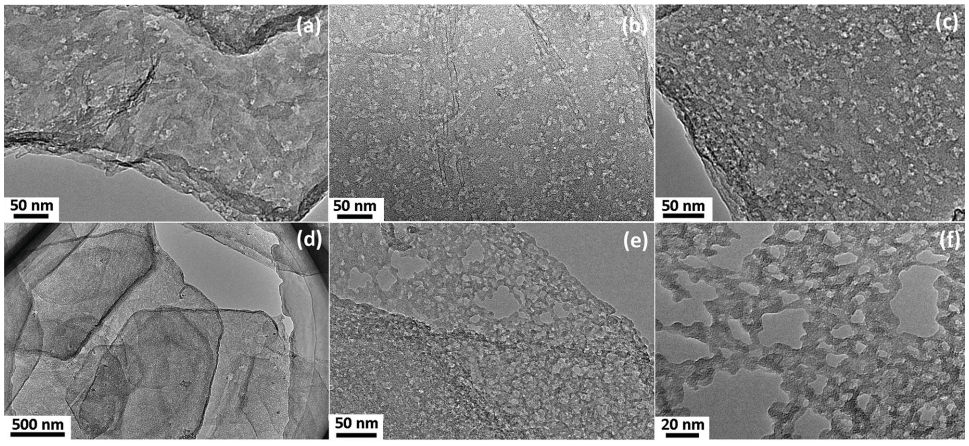

Figure 6. TEM images of a) CNM30-90, b) CNM60-90, c) CNM90-90, and d–f) CNM60-180.

highly porous CSs with seriously aggregated structure (Figure S5, Supporting Information). This result shows the unique and critical role of the LDO template in effectively preventing aggregation of carbon thin sheets. Moreover, the random distribution of large mesopores that is quite common for the CNMs disappears completely. The N_2 adsorption characterization reveals that the CS60-90 sample has a slightly decreased SSA of 1222 m^2 g^{-1}, but displays nearly identical PSD as compared with the CNM60-90 (Figure 3b). Given that CS60-90 was obtained by removing Fe_2O_3 and LDO prior to the thermal annealing, the above results clearly demonstrate that the abundant micro- and mesopores in the carbon layers are replicated from the LDO template during the CVD process, while the random distribution of large mesopores in the carbon thin sheets are created by Fe_2O_3 etching at the thermal annealing stage. These results were also supported by Raman spectrum (Figure S6, Supporting Information), where a higher I_D/I_G of CNM60-90 indicates more defects were introduced due to etching of carbon atoms with Fe_2O_3. Because of the absence of high-density in-plane large mesopores, the O/C ratio in CS60-90 dropped to 3.4 at% (Figure 3c, Figures S2 and S3, Supporting Information). Figure 7 compares the yields of the as-made CNM and CS prepared at different CVD time. Obviously, the lower yield of the CNMs at a given CVD time confirms the oxidation of carbon atoms by Fe_2O_3 particles at the annealing stage.

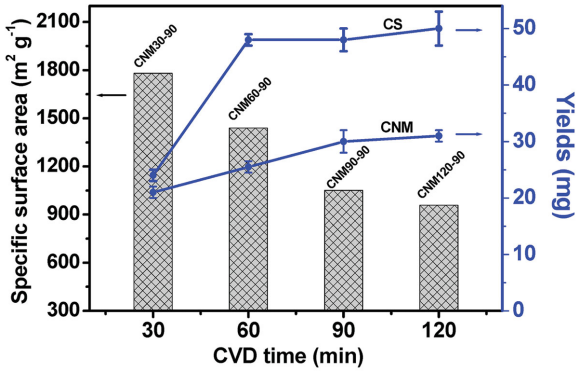

Figure 7. The dependence of SSA of CNM and product yields of CNM and CS on the CVD time. Both CNM and CS samples were thermally annealed at 800 °C for 90 min.

The unique structure enables the CNM to serve as an excellent electrode for high-rate supercapacitors simply because the in-plane large mesopores may help to improve the ion kinetics across the 2D carbon thin sheets. We assembled a symmetric supercapacitor using CNM60-90 as electrode, and compared its capacitive performance with CS60-90 electrode under the identical testing conditions using the best practice method recommended by Ruoff and Stoller.[48] **Figure 8**a shows the CV curves of the CNM60-90 and the CS60-90 electrodes at a scan rate of 50 mV s^{-1}. The CV profile for the CS60-90 is nearly ideal rectangular, suggesting a predominant ion adsorption at the electrode–electrolyte interface because the low content of functional groups (O/C ratio of 3.4 at%) contributes less to the pseudocapacitance.[38,43] However, in the case of the CNM60-90 capacitor, the CV profile exhibits an enhanced current response with a wide reversible hump in the voltage range of 0–0.7 V, suggesting that the charges are stored via both ion adsorption and Faradic redox reaction. Considering that CNM60-90 and CS60-90 have comparable SSA (1440 vs 1222 m^2 g^{-1}) and similar hexagonal morphology (Figure S5, Supporting Information) but with different O/C ratios (6.9 vs 3.4 at%), the area difference as indicated in Figure 8a can be ascribed to the contribution of pseudocapacitance from the oxygen functional groups in the CNM60-90. The pseudocapacitance accounts for ≈15% of the total capacitance of the CNM60-90 at the scan rate of 10 mV s^{-1}, and this value remains nearly unchanged while increasing the scan rate up to 500 mV s^{-1}. Figure 8b plots such pseudocapacitance at various scan rates. Interestingly, the linear increase of the pseudocapacitance with the scan rate suggests that the functional groups at the edges of the large mesopores can be fully accessed by the electrolyte ions even at a high scan rate of 500 mV s^{-1}. This result clearly demonstrates that these large mesopores in CNM60-90 has offered additional ion pathways that help to potentially accelerate the ion transport across the 2D plane of the carbon thin sheets, thus leading to an improved pseudocapacitance contribution from the oxygen-containing functional groups.

Figure 9a shows the CV profiles of the CNM60-90 electrode over a wide range of scan rates. In spite of the ≈15%

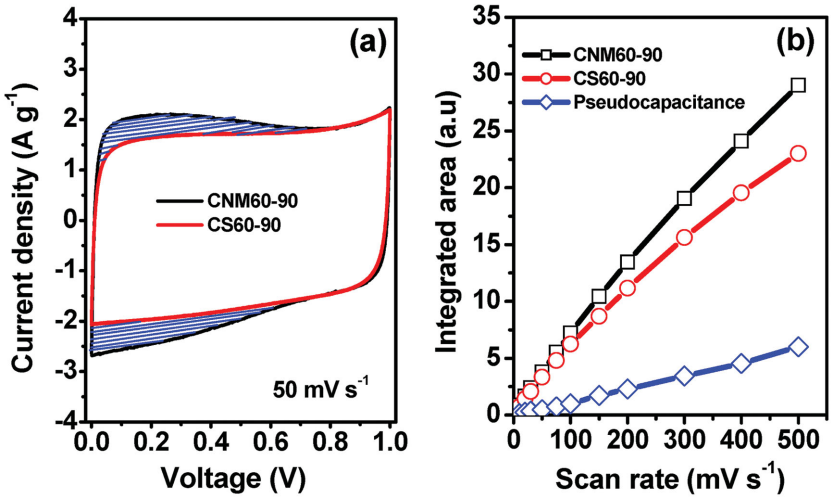

Figure 8. a) Comparative CV curves of CS60-90 and CNM60-90 capacitors at scan rate of 50 mV s^{-1} in 6.0 M KOH electrolyte, and b) the variation of the integrated area in panel (a) at different scan rates.

pseudocapacitance involved, the CNM60-90 capacitor displays a quasi-rectangular CV curve even at a high scan rate of 500 mV s^{-1}. Such an ideal capacitive behavior demonstrates its high-rate capacitive performance. Figure 9b shows the galvanostatic charge–discharge curves of the CNM60-90 capacitor at different charge rates. The symmetric charge and discharge curves reveal an ion adsorption and a reversible redox reaction at the electrode–electrolyte interfaces. Moreover, the CNM60-90 capacitor exhibits an extremely smaller voltage drop (IR drop) of 0.038 V at a current density of 5.0 A g^{-1} (Figure S7, Supporting Information). Obviously, the smaller IR drop of CNM60-90 reflects a smaller internal resistance due to the presence of a large number of holes in carbon thin sheets, which potentially accelerate the ion transport across the 2D carbon planes. The specific capacitance of the CNM60-90 at 0.25 A g^{-1} is 182 F g^{-1}, and it remains 70% of its initial capacitance at a current density of 30 A g^{-1} (128 F g^{-1}) (Figure 9c). In contrast, the CS60-90 electrode only shows a capacitance retention of 65% due to its larger ion diffusion resistance.

The ion transport properties of the electrolyte ions within the electrode were probed by electrochemical impedance spectroscopy (EIS). Figure 9d compares the Nyquist plots of the CNM60-90 and the CS60-90 capacitor in 6.0 M KOH electrolyte. Both show vertical lines in the low-frequency range, confirming primary contribution of electrostatic ion adsorption. In the middle-frequency range (inset in Figure 9d), the large Warburg region observed for CS60-90 capacitor reveals a slow transport of the electrolyte ions because of the lack of large ion pathways in the carbon sheets. This observation is consistent with its larger IR drop (Figure S7, Supporting Information) and inferior capacitance retention in Figure 9c. The dependence of phase angles on frequency is shown in Figure 9e. For both supercapacitors, the phase angles close to −90° at very low frequency suggests an ideal capacitive behavior. The characteristic f_0 at −45° marks the points where the capacitive behavior starts to transit into the resistive behavior.[49,50] The f_0 of the CNM60-90 and the CS60-90

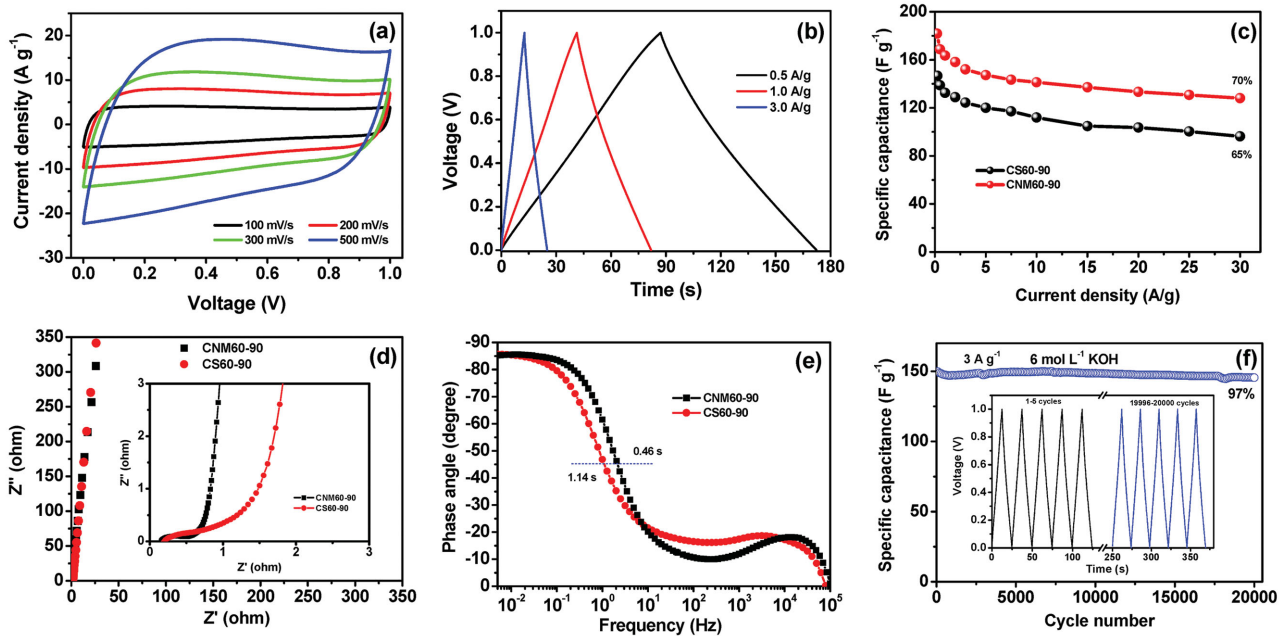

Figure 9. Capacitive performance of CNM60-90 and CS60-90 capacitor in 6.0 M KOH electrolyte. a) CV curves of CNM60-90 at various scan rates. b) Charge–discharge profiles of CNM60-90 capacitor. c) Comparative capacitance retention, d) Nyquist plots, and e) Bode plots of phase angle verses frequency. f) Cycling stability of CNM60-90 capacitor at current density of 3.0 A g^{-1} with inset showing the charge–discharge curves at first and last five cycles.

capacitor were measured to be 2.17 and 0.88 Hz (Figure S8, Supporting Information), corresponding to a time constant τ_0 (=1/f_0) of 0.46 and 1.14 s, respectively (Figure 9e and Figure S8, Supporting Information). Note the τ_0 of the CNM60-90 is much smaller than 4–5 s of chemically derived graphene-based capacitors,[17,51] and even comparable to 0.17 s of holey graphene capacitor.[21] Given that pseudocapacitance usually involves Faradic reaction with response time typically longer than double-layer capacitance, the very short time constant of the CNM60-90 clearly demonstrates the crucial role of in-plane large mesopores in greatly promoting the ion kinetics in the interior of the electrodes.

Apart from the high-rate performance, the CNM60-90 also exhibits an excellent cycling stability with 97% capacitance retention after 20 000 cycles of consecutive charge–discharge at 3.0 A g^{-1} (Figure 9f). The CV profiles at different cycling stages (Figure S9, Supporting Information) and the nearly identical charge–discharge curves (inset in Figure 9f) further confirm its electrochemical stability. It should be noted that for most of the pseudocapacitive materials that are loosely connected on conductive carbon substrates via weak electrostatic interactions or π–π attractions, they usually suffer from capacitance decay due to poor electrical connections and mechanical disintegrations arising from continuous volume change in charging/discharging process. Whereas, the pseudoactive oxygen functional groups that are covalently bonded to the carbon atoms can eliminate the large volume change to some degree, and therefore helps to maintain the structure integrity during the repeated cycling. This structure advantage is of importance for achieving a stable electrochemical property which is highly demanded for electrochemical energy storage devices.

3. Conclusion

Thin-sheet hexagonal carbon nanomesh has been prepared by a CVD method with LDO as sacrificial template and ferrocene as carbon precursor. The carbon nanomesh features a uniform distribution of micro- and mesopores with a pore size of 1–6 nm and large mesopores with a pore size of 10–50 nm. The micropores and smaller mesopores are replicated from the LDO template during the CVD process, while the large mesopores are created by etching away some carbon atoms around the Fe_2O_3 particles in the thermal annealing stage. The density and geometry of the large mesopores in the carbon thin sheets are closely related to the CVD time and the annealing conditions. The in-plane large mesopores serve as fast ion channels across the carbon thin sheets, which helps to greatly accelerate the ion kinetic in the interior of the electrode. As a result, an improved capacitive performance, evidenced by an enhanced specific capacitance, short time constant, good rate capability and excellent cycling performance has been achieved. The template CVD method reported here would open up a new avenue to functional carbon nanomesh materials for applications in fuel cells, electrochemical energy storage and conversion.

4. Experimental Section

CNM Preparation: The hexagonal flake-like MgAl-LDH with a lateral size of 2–4 μm was prepared following a method as described previously.[52] Typically, 0.77 g of $Mg(NO_3)_2{\cdot}6H_2O$ and 0.56 g of $Al(NO_3){\cdot}9H_2O$ were added into 30 mL water containing 0.44 g of urea. The solution was magnetically stirred at room temperature for 30 min before hydrothermal treatment in 60 mL autoclave at 140 °C for 24 h. The products were collected by filtration, rinsing with copious water and ethanol and drying at 80 °C. The MgAl-LDO powder was obtained by heating the MgAl-LDH at 500 °C for 60 min.

Deposition of carbon on the MgAl-LDO was performed following our methods reported recently.[53] Briefly, 0.45 g of MgAl-LDO powder was put into a quartz boat in a quartz tube. The sublimation and pyrolysis of ferrocene were conducted in flowing N_2 at 120 and 500 °C in 30–90 min, respectively. Then, the carbon–LDO composite was subjected to further thermal annealing at 800 °C in flowing N_2 for different durations. The LDO template in the LDO/carbon composite was etched away by successive refluxing in 2 M HCl and 15% HF solution for 12 h. After filtration, washing with copious deionized water and ethanol, the product was collected and dried at 80 °C.

Characterizations: The samples were examined by field-emission scanning electron microscopy on FEI Quanta 600F equipped with an EDX, and transmission electron microscopy on JEOL-2100F at an accelerating voltage of 200 kV. Nitrogen adsorption–desorption isotherms were measured at 77 K on ASAP 2460 analyzer. The samples were degassed at 180 °C for 6 h prior to the measurement. The SSA of the samples were calculated using the Brunauer–Emmett–Teller (BET) method with the adsorption data at a relative pressure (P/P_o) range of 0.05–0.2. The total pore volumes were estimated at P/P_o = 0.99. PSD curves were calculated from the adsorption branch using the NLDFT model assuming the slit pore geometry. XPS spectra were collected on an AXIS ULTRA spectrometer (Kratos Analytical) using a monochromatized Al Kα X-ray source (1486.71 eV). FTIR profiles were recorded on a Brucher Tensor27 spectrometer with the KBr pellet technique in a wave number range of 400–4000 cm^{-1}. Raman spectra were measured on a Renishaw inVia Raman microscope with an excitation wavelength of 532 nm.

Electrochemical Measurements: The working electrode was prepared by mixing an active material (90 wt%) with carbon black (5 wt%) and polytetrafluoroethylene (5 wt%) in water. The slurry of the mixture was then painted between two pieces of nickel foam (1.0 cm^2) and pressed at 100 kg cm^{-2}. The mass loading for each electrode is about 1.4 mg cm^{-2}. A Swagelock-type two-electrode capacitor was configured with the active materials as symmetric electrodes and Celgard 3501 membrane as separator. The capacitive performance of electrode materials in 6 M KOH aqueous electrolyte was characterized by cyclic voltammetry, galvanostatic charge–discharge, and EIS on a Gamry Reference 3000 electrochemical workstation. The total capacitance of a supercapacitor was calculated from the galvanostatic discharge process according to the following equation: $C_{total} = I \times \Delta t/(\Delta V \times m)$, where I is the discharge current (A), Δt is the discharge time (s), ΔV is the voltage change (V) excluding the IR drop during the discharge process, and m is the total mass of the active material for both electrodes (g). The specific capacitance of the single electrode is thus calculated as $C_s = 4 \times C_{total}$. EIS measurement of a supercapacitor was performed with amplitude of 10 mV in a frequency range of 5 mHz to 100 kHz.

Supporting Information

Supporting Information is available from the Wiley Online Library or from the author.

Acknowledgements

This work was partly supported by the National Natural Science Foundation of China (Nos. 21373134 and 21361162004), the fundamental Research Funds for the Central Universities (Nos. GK201403005, GK201301002, and GK201501007), 111 project (B14041), the foundation of returned overseas scholar, MOE, Program for Key

Science & Technology Innovation Team (2012KCT-21), and Nature Science Foundation of Shaanxi Province (2013JM2001).

Received: May 16, 2015
Revised: June 24, 2015
Published online: August 3, 2015

[1] X. Peng, L. Peng, C. Wu, Y. Xie, *Chem. Soc. Rev.* **2014**, *43*, 3303.
[2] M. D. Stoller, S. Park, Y. Zhu, J. An, R. S. Ruoff, *Nano Lett.* **2008**, *8*, 3498.
[3] J.-H. Chen, C. Jang, S. Xiao, M. Ishigami, M. S. Fuhrer, *Nat. Nanotechnol.* **2008**, *3*, 206.
[4] Z. Niu, J. Chen, H. H. Hng, J. Ma, X. Chen, *Adv. Mater.* **2012**, *24*, 4144.
[5] Y. Zhao, J. Liu, Y. Hu, H. Cheng, C. Hu, C. Jiang, L. Jiang, A. Cao, L. Qu, *Adv. Mater.* **2013**, *25*, 591.
[6] M. F. El-Kady, R. B. Kaner, *Nat. Commun.* **2013**, *4*, 1475.
[7] M. F. El-Kady, V. Strong, S. Dubin, R. B. Kaner, *Science* **2012**, *335*, 1326.
[8] Y. Xu, K. Sheng, C. Li, G. Shi, *ACS Nano* **2010**, *4*, 4324.
[9] H. Bi, X. Xie, K. Yin, Y. Zhou, S. Wan, L. He, F. Xu, F. Banhart, L. Sun, R. S. Ruoff, *Adv. Funct. Mater.* **2012**, *22*, 4421.
[10] Z. Yan, L. Ma, Y. Zhu, I. Lahiri, M. G. Hahm, Z. Liu, S. Yang, C. Xiang, W. Lu, Z. Peng, Z. Sun, C. Kittrell, J. Lou, W. Choi, P. M. Ajayan, J. M. Tour, *ACS Nano* **2013**, *7*, 58.
[11] Y. Zhu, L. Li, C. Zhang, G. Casillas, Z. Sun, Z. Yan, G. Ruan, Z. Peng, A.-R. O. Raji, C. Kittrell, R. H. Hauge, J. M. Tour, *Nat. Commun.* **2012**, *3*, 1225.
[12] Z. Lei, Z. Liu, H. Wang, X. Sun, L. Lu, X. S. Zhao, *J. Mater. Chem. A* **2013**, *1*, 2313.
[13] J. Huang, J. Wang, C. Wang, H. Zhang, C. Lu, J. Wang, *Chem. Mater.* **2015**, *27*, 2107.
[14] J. Bai, X. Zhong, S. Jiang, Y. Huang, X. Duan, *Nat. Nanotechnol.* **2010**, *5*, 190.
[15] I. Jung, H. Y. Jang, J. Moon, S. Park, *Nanoscale* **2014**, *6*, 6482.
[16] Z. Fan, Q. Zhao, T. Li, J. Yan, Y. Ren, J. Feng, T. Wei, *Carbon* **2012**, *50*, 1699.
[17] H. Wang, X. Sun, Z. Liu, Z. Lei, *Nanoscale* **2014**, *6*, 6577.
[18] Y. Xu, C.-Y. Chen, Z. Zhao, Z. Lin, C. Lee, X. Xu, C. Wang, Y. Huang, M. I. Shakir, X. Duan, *Nano Lett.* **2015**, *15*, 4605.
[19] W. Yuan, Y. Zhou, Y. Li, C. Li, H. Peng, J. Zhang, Z. Liu, L. Dai, G. Shi, *Sci. Rep.* **2013**, *3*, 2248.
[20] W. Yuan, J. Chen, G. Shi, *Mater. Today* **2014**, *17*, 77.
[21] Y. Xu, Z. Lin, X. Zhong, X. Huang, N. O. Weiss, Y. Huang, X. Duan, *Nat. Commun.* **2014**, *5*, 4554.
[22] X. Sun, P. Cheng, H. Wang, H. Xu, L. Dang, Z. Liu, Z. Lei, *Carbon* **2015**, *92*, 1.
[23] X. Zhao, C. M. Hayner, M. C. Kung, H. H. Kung, *ACS Nano* **2011**, *5*, 8739.
[24] Z. Zeng, X. Huang, Z. Yin, H. Li, Y. Chen, H. Li, Q. Zhang, J. Ma, F. Boey, H. Zhang, *Adv. Mater.* **2012**, *24*, 4138.
[25] X. Liang, Y.-S. Jung, S. Wu, A. Ismach, D. L. Olynick, S. Cabrini, J. Bokor, *Nano Lett.* **2010**, *10*, 2454.
[26] Y. W. Zhu, S. Murali, M. D. Stoller, K. J. Ganesh, W. W. Cai, P. J. Ferreira, A. Pirkle, R. M. Wallace, K. A. Cychosz, M. Thommes, D. Su, E. A. Stach, R. S. Ruoff, *Science* **2011**, *332*, 1537.
[27] X. Wang, L. Jiao, K. Sheng, C. Li, L. Dai, G. Shi, *Sci. Rep.* **2013**, *3*, 1996.
[28] X. Han, M. R. Funk, F. Shen, Y.-C. Chen, Y. Li, C. J. Campbell, J. Dai, X. Yang, J.-W. Kim, Y. Liao, J. W. Connell, V. Barone, Z. Chen, Y. Lin, L. Hu, *ACS Nano* **2014**, *8*, 8255.
[29] D.-P. Yang, X. Wang, X. Guo, X. Zhi, K. Wang, C. Li, G. Huang, G. Shen, Y. Mei, D. Cui, *J. Phys. Chem. C* **2014**, *118*, 725.
[30] D. Zhou, Y. Cui, P.-W. Xiao, M.-Y. Jiang, B.-H. Han, *Nat. Commun.* **2014**, *5*, 4716.
[31] Y. Lin, K. A. Watson, J.-W. Kim, D. W. Baggett, D. C. Working, J. W. Connell, *Nanoscale* **2013**, *5*, 7814.
[32] G. Ning, Z. Fan, G. Wang, J. Gao, W. Qian, F. Wei, *Chem. Commun.* **2011**, *47*, 5976.
[33] Z. Chen, W. Ren, L. Gao, B. Liu, S. Pei, H.-M. Cheng, *Nat. Mater.* **2011**, *10*, 424.
[34] M.-Q. Zhao, Q. Zhang, J.-Q. Huang, G.-L. Tian, J.-Q. Nie, H.-J. Peng, F. Wei, *Nat. Commun.* **2014**, *5*, 3410.
[35] C. Cui, W. Qian, Y. Yu, C. Kong, B. Yu, L. Xiang, F. Wei, *J. Am. Chem. Soc.* **2014**, *136*, 2256.
[36] Z. Fan, Y. Liu, J. Yan, G. Ning, Q. Wang, T. Wei, L. Zhi, F. Wei, *Adv. Energy Mater.* **2012**, *2*, 419.
[37] M.-Q. Zhao, Q. Zhang, J.-Q. Huang, F. Wei, *Adv. Funct. Mater.* **2012**, *22*, 675.
[38] Z. Lei, L. Lu, X. S. Zhao, *Energy Environ. Sci.* **2012**, *5*, 6391.
[39] M.-Q. Zhao, X.-F. Liu, Q. Zhang, G.-L. Tian, J.-Q. Huang, W. Zhu, F. Wei, *ACS Nano* **2012**, *6*, 10759.
[40] M.-Q. Zhao, Q. Zhang, X.-L. Jia, J.-Q. Huang, Y.-H. Zhang, F. Wei, *Adv. Funct. Mater.* **2010**, *20*, 677.
[41] W. Tian, Q. Gao, Y. Tan, Y. Zhang, J. Xu, Z. Li, K. Yang, L. Zhu, Z. Liu, *Carbon* **2015**, *85*, 351.
[42] Y. Li, Y. Zhao, H. Cheng, Y. Hu, G. Shi, L. Dai, L. Qu, *J. Am. Chem. Soc.* **2012**, *134*, 15.
[43] J. Yan, Q. Wang, T. Wei, L. Jiang, M. Zhang, X. Jing, Z. Fan, *ACS Nano* **2014**, *8*, 4720.
[44] X. Zhu, X. Song, X. Ma, G. Ning, *ACS Appl. Mater. Interfaces* **2014**, *6*, 7189.
[45] M. C. Schnitzler, A. S. Mangrich, W. A. A. Macedo, J. D. Ardisson, A. J. G. Zarbin, *Inorg. Chem.* **2006**, *45*, 10642.
[46] T. Palaniselvam, H. B. Aiyappa, S. Kurungot, *J. Mater. Chem.* **2012**, *22*, 23799.
[47] Y. Zhao, C. Hu, L. Song, L. Wang, G. Shi, L. Dai, L. Qu, *Energy Environ. Sci.* **2014**, *7*, 1913.
[48] M. D. Stoller, R. S. Ruoff, *Energy Environ. Sci.* **2010**, *3*, 1294.
[49] P. L. Taberna, P. Simon, J. F. Fauvarque, *J. Electrochem. Soc.* **2003**, *150*, A292.
[50] P. Cheng, S. Gao, P. Zang, X. Yang, Y. Bai, H. Xu, Z. Liu, Z. Lei, *Carbon* **2015**, *93*, 315.
[51] M. F. El-Kady, M. Ihns, M. Li, J. Y. Hwang, M. F. Mousavi, L. Chaney, A. T. Lech, R. B. Kaner, *Proc. Natl. Acad. Sci. USA* **2015**, *112*, 4233.
[52] G. Huang, S. Ma, X. Zhao, X. Yang, K. Ooi, *Chem. Mater.* **2010**, *22*, 1870.
[53] Z. B. Lei, N. Christov, X. S. Zhao, *Energy Environ. Sci.* **2011**, *4*, 1866.